

This is a postprint version of the following published document:

Torre-Gamarra, C. de la. Interplay between humidity, temperature and electrical response of a conductivity sensor based on a  $\text{La}_2\text{LiNbO}_6$  double perovskite. In: *Journal of Materials Chemistry A*, 6(13), Apr. 2018, Pp. 5430-5442

DOI: <https://doi.org/10.1039/c7ta09496e>

© 2018 Royal Society of Chemistry

# Interplay between humidity, temperature and electrical response of a conductivity sensor based on $\text{La}_2\text{LiNbO}_6$ double perovskite

C. de la Torre-Gamarra<sup>a</sup>, M. Woszczak<sup>a</sup>, B. Levenfeld<sup>a</sup>, A. Varez<sup>a\*</sup>, E. García-González<sup>b</sup>, E. Urones-Garrote<sup>c</sup>, V. Di Noto<sup>a,d</sup>.

<sup>a</sup> Universidad Carlos III de Madrid, Departamento de Ciencia e Ingeniería de Materiales e Ingeniería Química, Avda. Universidad 30, 28911, Leganés, Spain.

<sup>b</sup> Departamento Química Inorgánica, Facultad de Ciencias Químicas, Universidad Complutense, 28040 Madrid, Spain.

<sup>c</sup> ICTS-Centro Nacional de Microscopia Electrónica, Universidad Complutense, 28040, Madrid, Spain.

<sup>d</sup> Section of Chemistry for Technology, Department of Industrial Engineering, Università di Padova, Via Marzolo 1, 35131 Padova (Pd), Italy,

## Abstract

$\text{La}_2\text{LiNbO}_6$  perovskite has been prepared in polycrystalline form by a solid state reaction. Structural characterization by means of monochromatic X-ray and neutron powder diffraction (XRD and ND) and Rietveld refinement showed that the crystal structure belongs to the group of 1:1 B-site rock-salt ordered double perovskites with the most common tilting system amongst them  $a^-a^-b^+$  (S. G.  $P2_1/n$ ,  $a=5.61612(3)$ ,  $b=5.76645(2)$ ,  $c=7.94107(4)$  Å,  $\beta=90.276(2)^\circ$ ). Scanning Transmission Electron Microscopy (STEM) evidences that no cross substitution between Li and Nb is observed and that a remaining portion of lanthanum is randomly located in the projected positions of lithium. Impedance spectroscopy has been used to analyse the electrical-response properties of materials. Conductivity is strongly dependent on the relative humidity (RH), changing of about 3 orders of magnitude between 25 and 90% RH. However, no conductivity increase on RH% is observed when the lateral surfaces of the sensor are covered with paraffin. This confirms that adsorption of water by the sample plays a crucial role in modulating the conduction mechanism.  $\text{La}_2\text{LiNbO}_6$  also exhibits a very good durability, reproducibility, response time, hysteresis and dynamic linearity to be considered as a promising sensing material for a practical humidity sensor.

**Keywords:** Humidity sensor, Double Perovskite, Impedance spectroscopy, Neutron Diffraction, Proton conductor

## 1. Introduction

Humidity sensors have gained increasing interest in research because of their wide application in household and industry, such as manufacturing processes, home automation, food and pharmaceutical storage, automotive equipment or healthcare. For daily life utilization, relative humidity (RH), which is the ratio of the partial pressure of water vapour present in a gas to the equilibrium saturated vapour pressure of water at the same temperature, is commonly given as a humidity measurement.<sup>1</sup> For practical applications, a good humidity sensor must comply with several requirements like good sensitivity in a wide range of humidity and temperature, small hysteresis, negligible temperature dependence, short response time and low cost. RH humidity sensing materials are essentially ceramic-type or polymer-based materials. Ceramic materials offer some advantages with respect to polymers, due to their high chemical, physical, mechanical and thermal stability. In addition, they exhibit high potential for design miniaturization.<sup>2</sup> The most widely used materials as ceramic sensors are binary oxides, such as  $\text{Al}_2\text{O}_3$ ,<sup>3</sup>  $\text{TiO}_2$ ,<sup>4</sup>  $\text{CeO}_2$ ,<sup>5</sup>  $\text{SiO}_2$ <sup>6</sup> and ternary oxides such as spinels ( $\text{AB}_2\text{O}_4$ )<sup>7,8</sup> and perovskites ( $\text{ABO}_3$ ).<sup>9,10</sup> Although there is no one single material that fulfils all the requirements, perovskites are extensively used due to their desirable properties such as the linear response, the high sensitivity, the wide detection range, and the short response time.<sup>11</sup> A recent review of Blank *et al.*<sup>2</sup> summarizes the state of the art on ceramic humidity sensors and Tables 2 and 3 therein sum up the information about spinel and perovskite-type materials used. Most of them exhibit humidity sensitivity at relatively high temperatures (different ranges between 300 and 700° C) based on their semiconductor nature.<sup>12-14</sup> At room temperature, however, some porous perovskite oxides still demonstrate humidity sensitivity, e.g.,  $\text{BaMO}_3$  (with  $M = \text{Ti, Zr, Hf, or Sn}$ ).<sup>15,16</sup> More recently published results have shown that some of the  $\text{ABO}_3$ -type niobate perovskites possess excellent properties for humidity sensing applications. Examples include  $\text{NaNbO}_3$  nanofibers<sup>17</sup>,  $(\text{K, Na})\text{NbO}_3$  thin films<sup>18</sup>,  $\text{K}_{0.5}\text{Na}_{0.5}\text{NbO}_3$  powders<sup>19</sup>, and a layered perovskite-type niobate  $\text{A}_5\text{Nb}_4\text{O}_{15}$  ( $A = \text{Ba, Sr}$ ).<sup>20</sup> The functioning principle of all ceramic humidity sensors relies on the superficial water vapour adsorption. By water adsorption on the surface, the electrical properties would change and this change

includes the resistance, capacitance or electrolytic conduction. The adsorption mechanism of the water molecules on the surface of the ceramic oxides is well known and based on chemical adsorption (chemisorption), physical adsorption (physisorption) and capillary condensation processes.<sup>21</sup> In the water uptake of ceramic humidity sensors, the adsorbed water is condensed on the material surface/bulk and conduction will be carried out by the protons, which thus are the dominant charge carriers responsible for the electrical conductivity in perovskites when they are exposed to humidity. The electrical parameters of perovskites sensitive to water adsorption are the resistance, the capacitance or the electrolytic conduction. Thus, Impedance spectroscopy is a very powerful technique to detect changes in resistance and/or capacitance on humidity.<sup>3,22</sup>

In this manuscript, we present the results obtained in the structural and electrical characterization of the  $\text{La}_2\text{LiNbO}_6$  perovskite-type compound. It belongs to the family of analogous phases  $\text{La}_2\text{LiMO}_6$  (M= Mo, Re, Ta, Ir) and to the best of our knowledge it has not been reported before.<sup>23,24</sup> The perovskite here described was found previously as a secondary phase in the synthesis of the garnet-type solid electrolytes  $\text{Li}_5\text{La}_3\text{Nb}_2\text{O}_{12}$ .<sup>25</sup> Here we have prepared  $\text{La}_2\text{LiNbO}_6$  as a single phase material and we have studied its structural features by powder X-ray and neutron diffraction and high resolution scanning transmission electron microscopy (STEM). This compound belongs to the group of  $\text{A}_2\text{BB}'\text{O}_6$  perovskites, commonly termed double perovskites, which are obtained when a 1:1 B-site ordering occurs by means of different mechanisms.<sup>26</sup> This B-B' 1:1 ordering can also involve octahedral tilting and  $\text{La}_2\text{LiNbO}_6$  belongs to this category. Detecting the octahedral tilt is based on oxygen positions and can be difficult to distinguish by X-ray diffraction (XRD), especially when heavy elements are present. In this sense, neutron diffraction is a powerful tool to analyze the crystal lattice and the position of light elements like oxygen and lithium. The electrical response of the material was studied by impedance spectroscopy. The material presented a sensitive response to conductivity when exposed to different humidity conditions. The experimental results clearly indicate that the remarkable low temperature conductivity observed in this system is associated with surface protonic conduction. The aim of this paper is to prepare and demonstrate that the proposed perovskite-type compound is a new promising sensing material for the development of practical ceramic humidity sensors.

## 2. Experimental

## 2.1 Synthesis

The compound  $\text{La}_2\text{LiNbO}_6$  was prepared by conventional solid-state reaction in air from stoichiometric amounts of high purity  $\text{Li}_2\text{CO}_3$  (99.99%, Sigma-Aldrich),  $\text{La}_2\text{O}_3$  (99.99%, Sigma-Aldrich) and  $\text{Nb}_2\text{O}_5$  (99.9%, Sigma-Aldrich).  $\text{La}_2\text{O}_3$  was previously heated at 800 °C for 12 h.  $\text{La}_2\text{O}_3$  shows a high tendency to carbonation and hydration. Indeed, when the container of a high purity  $\text{La}_2\text{O}_3$  reagent is opened to the air for a very short time, it immediately adsorbs  $\text{CO}_2$  and  $\text{H}_2\text{O}$ . Thus, before its use, a pre-heating process at 800 °C is necessary in order to eliminate any traces of carbonates and water. In order to avoid lithium loss during the synthesis, 15 % wt. of  $\text{Li}_2\text{CO}_3$  excess was added to the stoichiometric ratio and the heating rate used in the thermal treatments was 1 °C  $\text{min}^{-1}$ . After mixing in an agate mortar, the powder was heated at 700°C during 10 h for calcination. Once cooled down to room temperature, a secondary reground was carried out and the powder was pressed under 200 MPa and heated at 800°C for 10 h. Finally, the sample was ground again, uniaxially pressed into pellets and sintered at 1100 °C for 10 h.

## 2.2 Characterization

Sample was first characterized by means of room temperature XRD for phase identification and in order to determine phase purity. Data were collected in Bragg–Brentano reflection geometry ( $\theta/2\theta$ ) on an X'Pert MPD PRO (PANalytical B.V.) diffractometer (45 kV, 40 mA), using filtered  $\text{CuK}\alpha 1$  radiation ( $\lambda = 1.540598 \text{ \AA}$ ) with a Ge (111) primary monochromator. A divergence and anti-scattering slit of 0.5° and 1°, respectively, mounted in the pathway of the incoming beam was adopted. The diffracted beam passed through a soller slit (0.02 rad) before arrive to a multichannel X'Celerator RTMS (real-time multiple strip) detector. The samples were mounted as thin layers from acetone slurries onto zero background sample holders (Si (510)) and measured on a PW3064/60 sample spinner stage at 8 revolutions per second. The data were obtained between 5° and 110°  $2\theta$  in steps of 0.008°.

For the structural refinement, NPD experiments were carried out at room temperature (295 K) and at 3.5 K in the high resolution D2B neutron diffractometer ( $\lambda = 1.910 \text{ \AA}$ ), at the ILL-Grenoble, France. The powder samples (about 4 g) were contained in a vanadium cylinder. Data were collected between 5 and 160°  $2\theta$  with a scan step of 0.02° (4h). The

refinement of the crystal structure was performed by the Rietveld method<sup>27</sup> by using the FULLPROF refinement program.<sup>28</sup> A pseudo-Voigt function was chosen to describe the line shape of diffraction peaks. In a first stage, scale factors, background coefficients, zero-point error, width and peak-shape parameters were determined. After that, positional parameters, site occupation factors and thermal factors of atoms were refined.

The microstructure of sintered samples was analysed with a Philips XL30 scanning electron microscope operating at 10 kV. The microscope is equipped with a backscattered-electron detector (BSE) and an energy-dispersive analyser (EDAX 4i).

Samples for transmission electron microscopy (TEM) were ultrasonically dispersed in n-butanol and transferred to carbon-coated copper grids. Selected area electron diffraction (SAED) and high-resolution transmission electron microscopy (HRTEM) were performed on a JEOL JEM300F electron microscope by working at 300 kV (point resolution of 0.17 nm). Crystal-by-crystal chemical microanalysis was performed by energy-dispersive X-ray spectroscopy (XEDS) with an ISIS 300 X-ray microanalysis system (Oxford Instruments). High angle annular dark field (HAADF) and annular bright field (ABF) scanning TEM (STEM) work was performed on an ARM200cF microscope, fitted with a condenser lens aberration corrector (point resolution in STEM mode of 0.08 nm). HAADF images were acquired with an inner acceptance angle of 90 mrad and ABF ones with a collection angle of 11 mrad. The same ARM200cF microscope was employed for electron energy-loss spectroscopy (EELS) experiments, since it is fitted with a GIF Quantum-ER spectrometer. EELS mapping was performed with a collection semi-angle  $\beta \sim 30$  mrad, 1 eV per channel dispersion and a collection time for each spectrum of 0.1 seconds. La-M<sub>4,5</sub> and Nb-L<sub>2,3</sub> edge signals were chosen for mapping.

Thermo-gravimetric analysis of proton exchanged samples was performed between 30 and 900 °C, using a TA PerkinElmer Pyris 1 apparatus, with a heating rate of 10 °C min<sup>-1</sup> under a dynamic nitrogen atmosphere flowing at 50 ml min<sup>-1</sup>. For each measurement, approximately 10 mg of the powder was weighed in a platinum crucible.

Electrical measurements were performed by Electrochemical Impedance Spectroscopy on a pellet with a diameter of 8 mm and a thickness of 2 mm. Gold electrodes were painted onto the surfaces of the pellet. The electrical measurements were performed on a parallel-plate capacitor configuration in air atmosphere. Before performing the measurements, the sample was heated for 1 h at 800 °C and quickly cooled down to room temperature. This

process, which eliminates any adsorbed traces of impurities, is a suitable chemical reset of the material. Indeed, it allows performing measurements in a reproducible way and confirms that the proposed perovskite is a chemically and thermally stable sensing material to use in a sensor device

Measurements were performed using an impedance analyser (Solartron 1260) in the frequency range from 0.1 Hz to 10 MHz. Impedance data were corrected for pellet geometry and capacitance of the conductivity jig. Measurements at different temperatures (RT-70 °C) and humidity (25-90% RH) conditions were performed in a Binder KMF 115 (E5.2) constant climatic chamber. In all cases the conductivity was measured after 20 min of equilibrium at each temperature and humidity conditions. By using this method, the RH and temperature could be controlled up to  $\pm 1\%$  and  $\pm 1^\circ\text{C}$  respectively. Durability of proposed material was evidenced a) by using a sensor based on proposed perovskite materials, which have been operating for one year; and b) by testing its response at 50 RH% and  $T = 50^\circ\text{C}$  for one week.

The impedance data analysis was performed using the ZView2 program.<sup>29</sup>

The ionic conductivity of the sample at room temperature is determined by the equation:

$$\sigma = \left(\frac{1}{R}\right) \left(\frac{l}{A}\right) \quad (1)$$

where R is the resistance value obtained from the intersection in Nyquist plot of the impedance curve with the axis of the real component of the impedance and  $l$  and  $A$  are the thickness and the area of the pellet, respectively.

The response time of the sensor is measured at  $T = 20^\circ\text{C}$  and at the RH% of: 1) the environment (35%); and 2) the three saturated salt solutions of LiCl (11%), NaCl (75%) and  $\text{KNO}_3$  (95%). The response time is determined by measuring on time the real component of the conductivity at 1 kHz (in the plateau) as follows. First the conductivity at the RH% of the environment is measured. Then, the sensor is rapidly inserted into a closed vessel containing the desired salt saturated solution. After this measurement, the sensor is rapidly opened to the environment. This procedure was repeated for all the three investigated saturated salt solutions. The response time was evaluated by fitting the profiles of the logarithm of the decay of the conductivity on time with exponential functions.

The dynamic linearity of the device is obtained by plotting the values of the average conductivities on the RH%. Conductivity values are determined from the plateaus of the response signals.

### 3. Results and Discussion

#### 3.1 Structural characterization

Polycrystalline white powder of  $\text{La}_2\text{LiNbO}_6$  was successfully obtained by solid-state reaction. The sintered  $\text{La}_2\text{LiNbO}_6$  sample presents a high homogeneous microstructure with equiaxial grains in the range 1–4  $\mu\text{m}$  large. The absence of particles with different contrast in the BSE micrograph (figure S1 of Supporting Information) is in agreement with the high purity of this sample. In spite of the relatively high porosity of the sample, grains are well connected between them.

Figure 1-a shows the room temperature powder XRD pattern, of the sample with the nominal composition of  $\text{La}_2\text{LiNbO}_6$ . The pattern is characteristic of a distorted perovskite showing well-defined superstructure reflections. All diffraction maxima can be indexed in a monoclinic unit cell with  $P2_1/n$  symmetry (S.G. 14) (Glazer tilt system  $a^-a^+b^+$ ), and cell parameters  $a \approx b \approx a_p\sqrt{2}$ ,  $c \approx 2a_p$ , where  $a_p$  is the lattice parameter of the aristotype  $Pm3m$  perovskite, in agreement with a double perovskite (DP) with the general formula  $\text{A}_2\text{BB}'\text{O}_6$ . No impurity phases were detected from XRD data.

The structural refinement was carried out from the NPD patterns acquired at both 3.5K and RT. The structure of  $\text{La}_2\text{NiRuO}_6$ <sup>30</sup> isostructural with  $\text{La}_2\text{LiMoO}_6$ <sup>23</sup> was used as a trial model: B and B' cations were located on special positions  $2c$  Li (0, 1/2, 0) and  $2d$  Nb (1/2, 0, 0), whereas the A-site cation (La) and each of the three non-equivalent oxygen atoms were located on general positions  $4e$  (x,y,z) of the  $P2_1/n$  Space Group. Observed, calculated, and difference profiles of ND patterns collected at 3.5 K are shown in Figure 1-b. In a first step, occupancy factors of different atoms were constrained to be equal to nominal composition. Afterwards, disordering between Li and Nb in the two positions was considered. Atomic coordinates, occupancy factors and equivalent isotropic displacements derived from the refinement are given in Table I. Results confirm the ordered distribution of Li-Nb (see below). The lattice parameters, relevant bond lengths and bond angles, besides agreement factors of the refinement are listed in Table II. Figure 1-c shows the deduced structural model for  $\text{La}_2\text{LiNbO}_6$ . The lattice parameters  $a \approx \sqrt{2}a_p$ ,



$b \approx \sqrt{2}a_p$ ,  $c \approx 2a_p$  indicate a type of distortion which is usually observed in  $A_2BB'O_6$  perovskites when the tolerance factor  $t$  becomes small,  $t \leq 0.97$  ( $t = 0.929$  calculated for  $\text{La}_2\text{LiNbO}_6$ ). In simple perovskites, optimization of the A-O bonding is the driving force for tilting and it is favoured when the fit of the A cation in the cubic network of corner sharing octahedral is poor. In  $\text{La}_2\text{LiNbO}_6$ , alternating  $\text{LiO}_6$  and  $\text{NbO}_6$  octahedra display an in-phase octahedral tilt along c-axis and an antiphase tilt along [100] and [010] directions of the aristotype cubic perovskite, tilt system  $a^-a^+b^+$  in Glazer notation. The most common group for this distortion in disordered perovskites is the orthorhombic  $Pnma$  that gives the monoclinic  $P2_1/n$  space group in the presence of extended cation ordering. The two factors commonly affecting ordering are present, *i.e.*, the difference in the B and B' cation oxidation states and their relative ionic size.<sup>31,32</sup> Corner-sharing  $\text{LiO}_6$  and  $\text{NbO}_6$  octahedra, alternate in a B/B' "rock salt" scheme. The refinement showed that  $\text{La}_2\text{LiNbO}_6$  is a 1:1 ordered perovskite in which Li and Nb exhibit long range order along c-axis with basically no mixing over the two crystallographic sites (less than 2% at 3.5K). Thus, corner-sharing  $\text{LiO}_6$  and  $\text{NbO}_6$  octahedra alternate along c-axis. Both  $\text{LiO}_6$  and  $\text{NbO}_6$  octahedra are slightly distorted, that of alkaline ion being more distorted. Moreover, a displacement of the Li and Nb atoms from the centre of their octahedra was detected and three different Nb-O and Li-O distances were observed. As a consequence of the octahedral tilting, some oxygen atoms are displaced away from the La at distances  $> 3\text{\AA}$  and the coordination of La changed from 12 to 8; consequently, La atoms are into bicapped trigonal prisms between octahedra packing. The average tilting angles estimated as  $\phi = (180 - \theta)/2$ , where  $\theta = \langle \text{Nb-O-Li} \rangle$ , were  $15.55^\circ$  and  $15.36^\circ$  at 3.5K and RT, respectively.

### 3.2 Transmission Electron Microscopy

Sample was further investigated by transmission electron microscopy. Figure 2-I shows the selected area electron diffraction (SAED) patterns of different crystals of the sample taken along the [100] (a), [010] (b) and [001] (c) zone axes. All diffraction maxima can be assigned on the basis of a monoclinic  $P2_1/n$  cell compatible with the ordered disposition of Li and Nb in the B sublattice.

The atomic distribution, as well as the structure at the atomic scale, was further investigated by HAADF and ABF STEM imaging. Under HAADF imaging conditions,

the contrast of the obtained images is roughly proportional to the square of the atomic number  $Z$  of the species, so it is possible to determine the elemental distribution at the atomic level as well as small local chemical variations. Figure 2-II shows the simultaneous HAADF (left) and ABF (right) STEM images of a crystal in the [010] projection.

Image contrast in the HAADF-STEM micrograph show groups of three dark spots ordered along [001] in the (001) planes. A ball and stick structural model in which oxygen atoms have been omitted, is overlapped to the experimental image as a help for the eye where green, blue and red balls correspond to lanthanum, lithium and niobium atoms, respectively. Under  $Z$ -contrast conditions, light atoms such as oxygen ( $Z=8$ ) or lithium ( $Z=3$ ) cannot be detected, so the image contrast is interpreted on the basis of the atomic sequence ...La-Nb-La-Li-La-Nb-La-Li... in the (001) planes, where columns of lithium atoms have no contribution to the image contrast. Correspondence between image contrast and projected model shows that the groups of three dark spots resemble the sequence \_\_\_La-Nb-La\_\_\_La-Nb-La\_\_\_ and the space between the triads matches with the projected position of lithium atoms. It can be appreciated that ordering occurs in the long range along the crystals. In order to evaluate whether or not cross substitution exists in certain extension between Li and Nb, atomic resolution elemental mapping from the Nb-L<sub>2,3</sub> and La-M<sub>4,5</sub> edge EELS signals have been recorded from a selected area (green square in Figure 3a). Projected ball and stick structural model displaying niobium and lanthanum atomic positions have been included in order to show the niobium sites. The excellent match between niobium positions in the Nb map and niobium positions in the structure model provides evidence about the location of niobium atoms only in one crystallographic position, excluding the possibility of partial cross substitution Li-Nb. La map reproduce the distribution of La atomic columns but, in addition, signal extends along [001], thus overlapping with the position corresponding to the columns of lithium atoms. A close observation of the HAADF image clearly shows a faint white contrast in most of the projected positions of Li columns. Figure 3b shows the HAADF image of a crystal in the [010] projection and the corresponding intensity scan profiles obtained along the selected lines. Profiles along [100] and [001] clearly show a nonzero intensity in the projected positions of lithium columns (long arrows). In addition, intensity profile along [100] shows that extra contrast is shifted from the central position thus giving rise to an ordered alternation of short and long distances along [100]. The same information

is obtained from the analysis of the HAADF images acquired in the [100] projection (Figure 3c): niobium map reproduces the projected niobium sites but lanthanum map again shows lanthanum signal extended along [001] thus overlapping with lithium atomic positions. The intensity profile analysis along [010] shown on Figure 3d reveals a clear contrast in the lithium positions as well but in this orientation this extra contrast is placed in the central positions between two niobium atoms.

Provided that light atoms such as oxygen ( $Z=8$ ) or lithium ( $Z=3$ ) cannot be detected under Z-contrast conditions, the observed contrast must be due to other of the existing species. Data from the elemental mapping point towards lanthanum contribution. It is important to insist on the fact that the contrast is weak and therefore the relative amount of lanthanum contributing to it must be small.

As mentioned before, the contrast under HAADF conditions is chemically sensitive but the signal scales strongly with atomic number and the weak scatterers lithium and oxygen atoms make an insignificant contribution to the image contrast. In this sense, ABF imaging was performed at the same time as HAADF. Under ABF conditions, the contrast has a low scaling rate with  $Z$  so it is a strong technique for simultaneous imaging of light and heavy elements. Figure 2-II (right) shows the ABF-STEM image of a crystal in the [010] projection. The projected structure model has been included in the image display, where niobium and lithium correspond to red and blue octahedra, respectively. Tilting along [100] direction can be easily observed and it perfectly matches with the atomic contrast in the image. The O-Nb-O line can be clearly recognized and niobium octahedral tilting identified. Lithium octahedra tilting become also visible in spite that lithium atoms contribute with a very faint contrast. However, some of the lithium positions give a strong contrast (see marked area on the image) and it points to the previous observations on the HAADF images, indicating that partial occupation of these positions by a strong scatterer than lithium is taking place.

### **3.3 Thermal characterization**

The TGA profile of Figure 4 shows four thermal mass eliminations (I, II, III and IV). Process I, detected at  $T < 300^{\circ}\text{C}$  (see derivative curve of Figure 4), corresponds to the elimination of 0.047wt% of water molecules forming, by physisorption phenomena, the first solvation shell of the chemically bonded water molecules.

II event (0.068wt%) peaking at  $T = 350^{\circ}\text{C}$ , shows the typical behaviour of a mass elimination event involving a chemical reaction. Thus, it is assigned to the mass loss of water fraction chemically bonded on the surface of the perovskite material.

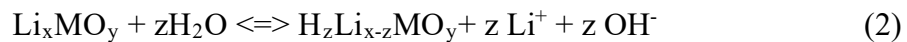
III and IV mass eliminations are attributed to the water elimination processes occurring owing to crosslinking phenomena taking place on the surface of  $\text{La}_2\text{LiNbO}_6$  perovskite materials. It should be observed, that when water is chemically coordinated to a metal ion (chemically bonded water) it is transformed easily into a hydroxyl group with a consequent release of a proton. Indeed, the presence of a thin layer of physisorbed water molecules facilitates the  $\text{H}^+$  dissociation and improves its delocalization. In physisorbed water layers a significant increases of the conductivity is revealed. For this reasons, it should be highlighted that, in order to develop an efficient RH% sensor it is necessary that the sensing perovskite material presents both I and II events and that the fraction of water characterizing these phenomena rises in the order  $\text{II} > \text{I}$ .

### 3.4 Electrical characterization

A typical impedance data set measured in air at RT is shown in Figure 5-I. The Nyquist impedance diagram (Figure 5-I-1) shows a single almost undistorted semicircle with an associated capacitance of  $\sim 90$  pF and is, therefore, attributed to the bulk resistance of the sample. In the low frequency region an inclined spike is clearly distinguished with an associated capacitance of  $\sim 300$   $\mu\text{F}$ . This value is typical of a double-layer capacitance associated to an ionic conductor with blocking electrodes. The frequency dependent conductivity (Figure 5-I-2) comprises two regions, the plateau at low frequencies, and the dispersion at high frequencies. The plateau of the real component of conductivity ranges from about  $10$  to  $10^4$  Hz and exhibits conductivity values which are constant and coincident with the overall conductivity of the sample. The  $M''/Z''$  plots shown in Figure 5-I-3, display a single peak almost coincident in frequency ( $M''$  peaks at a slightly higher frequency than that of the  $Z''$  peak). This indicates that the electric response can be represented by a single parallel RC element. The capacitance plot, (Figure 5-I-4) shows a plateau in the high frequency wing with values of the order of pF, and a dispersion at lower frequencies. In addition, in Nyquist plot, the interception of  $Z^*$  profile with the abscissa at the low frequency shows a bulk ion conductivity of  $1.598 \cdot 10^{-7} \text{ S cm}^{-1}$ . A value that is quite far from the conductivity values typically observed in the best ion conductors.

To study the electric response of this ion conductor, the temperature dependence of its conductivity was investigated. In a first stage, measurements are carried out in air and without humidity control and data were acquired on sample heating and cooling processes (Figure 5-II-1 and 2, respectively). Prior to each measurement, the sample is quenched from 800 °C to room temperature to eliminate any possible adsorbed water (chemical reset of the sample). Surprisingly, the conductivity of the material drops dramatically as the temperature increases and then easily recovers upon cooling down to room temperature. This is not the expected behaviour for an ion conductor. This suggests that the charge migration in  $\text{La}_2\text{LiNbO}_6$ , likely occurs owing to a proton migration process in physisorbed water domains. These water domains are quickly formed by adsorption of water from the environment. It is well accepted that lithium migration in perovskites is a thermally stimulated process, as widely reported in common literature,<sup>33,34</sup> whilst in our hydrated material, as the temperature is raised, the conductivity decreases. This opposite behaviour suggests that in hydrated perovskites water plays a crucial role in modulating the long-range charge migration events. Therefore, it must be admitted that the conductivity mechanism of hydrated proposed material is different from that usually exhibited by dry perovskites. Results shown in figure 6 strongly support this interpretation.

The easy exchange reaction of mobile lithium cations by protons of water in Li-containing inorganic compounds such as LLTO perovskites<sup>35,36</sup> and  $\text{Li}_5\text{La}_3\text{Nb}_2\text{O}_{12}$ <sup>37</sup> garnet is a well-known phenomenon. In order to discard the occurrence of  $\text{Li}^+/\text{H}^+$  exchange reaction, the sample was immersed in deionized water and the pH variation was recorded over time. As shown in figure S2, the pH value basically does not change with the immersion time, unlike what occurs in the perovskite LLTO, where the pH value rise from 6 to 10 as a consequence of the  $\text{OH}^-$  ions released to the solution according the reaction,<sup>36</sup>



This observation confirms that Li ions located at B-site are not mobile.

### 3.4.1 Effect of humidity

Based on the above results, and looking for strong indications of humidity sensitivity of this material, impedance spectroscopy measurements were performed at different relative

humidity values and at a constant temperature, ranging from 30 to 70 °C. Figure 6 shows the impedance data set obtained at 60 °C and relative humidity (RH) ranging from 25 to 90%. Part (a) corresponds to the Nyquist plot and (b) and (c) show the real component of conductivity and capacitance plots versus frequency, respectively. In these conditions impedance is dominated by a single arc. A significant increase of conductivity occurs in the measured humidity range. This increase of  $\sigma'$  in three orders of magnitude from 25 to 90% RH (see also below) proves that the material is endowed with a very high sensitivity toward humidity changes at all temperatures. Furthermore, the conductivity of the material is not influenced by the frequency in a wide frequency range. From the technological point of view this is a very promising condition in order to develop sensor based on cheap electric transducers operating at different frequencies.

The dependence of conductivity on RH% of the  $\text{La}_2\text{LiNbO}_6$  perovskite pellet (Figure 7a) presents two linear regions (I and II) delimited by the value of  $\text{RH}\% \approx 62\%$  and is fitted by least-square methods using the equation 1

$$\log \sigma = \log \sigma_0 + S \cdot (R. H. \%) \quad (3)$$

where  $S = \frac{\partial \log \sigma}{\partial (R.H.\%)}$  is the sensitivity of the conductivity sensor and  $\sigma_0$  is the conductivity at  $\text{RH}\% = 0$ . The parameters determined in I and II regions are summarized in Table III. It should be highlighted that in I and II RH% response regions, the S values of the sensor based on  $\text{La}_2\text{LiNbO}_6$  perovskite are higher of at least five times with respect to values recently reported elsewhere for a layered perovskite-type based sensor.<sup>38</sup>

In region I, two groups of overlapped curves which share the same value of the intercept ( $\sigma_0$ ) are detected (Figure 7-b). The first group (A) consists of the curves at  $T < 45^\circ\text{C}$  while the second of those measured at  $T \geq 45^\circ\text{C}$  (B). It is observed that the sensitivity parameters in I exhibit very stable values for both the two groups of linear curves (see table III and Figure 7b). Thus, in terms of sensitivity and intercept stability, region I is the best one for the application of  $\text{La}_2\text{LiNbO}_6$  materials in practical conductivity RH% sensors. In region II, no clear dependence on temperature of the  $\sigma_0$  and S parameters is revealed (see Figure 7a and 7b), which indicates that in this region the proposed ceramic is very difficult to apply in practical automatized sensors. Furthermore, the analysis of Figure S3 clearly summarizes that  $\text{La}_2\text{LiNbO}_6$  is a very promising perovskite material for

the development of conductivity ceramic sensors for detection of RH% at  $T \geq 45^\circ\text{C}$  and  $\text{RH}\% > 62\%$ .

Results above discussed demonstrate that at  $T > 45^\circ\text{C}$  and  $\text{RH}\% > 62\%$  (B and I regions) the conductivity response is associated to the long range proton migration events, which occur within the first water solvation shell of physisorbed water molecules. This latter is directly interacting with the chemically bonded water molecules coordinating the metal ions on the surface of the ceramic material. In this case, it is expected that the thickness and the volume of the water solvation shell, where the protons are delocalized after dissociation from the chemically bonded water molecules, are constant and depends on RH%, respectively. Therefore, in I and B regions, as expected, no dependence of the  $\sigma_0$  and S parameters on temperature is registered (Figure 7b). These evidences are perfectly in accordance with results determined by TGA analysis and indicate that event I corresponds to the amount of water molecules in the first solvation shell, *i.e.* the physisorbed water molecules operating in the sensor in B and I regions. To further confirm this interpretation, impedance spectra were collected on a gold electroded  $\text{La}_2\text{LiNbO}_6$  pellet that was previously dried at  $800^\circ\text{C}$  and quenched in dry atmosphere. The lateral pellet surfaces (free of gold electrode) were covered with a paraffin film inside a dry box. Subsequently, impedance spectroscopy measurements were undertaken in a broad range of RH (0-90%) into the humidity chamber at  $50^\circ\text{C}$ . Similar experiments were previously performed for micro and nanometric grain size YSZ when studying the increase in conductivity at low temperature in wet conditions.<sup>39,40</sup> The results are shown in Figure S4. It can be observed a large dispersion in the low frequency region where the plateau associated to dc conductivity is located, indicating that within the instrumental precision these values are ranging between  $10^{-8}$  and  $10^{-10}$   $\text{S}\cdot\text{cm}^{-1}$ . These latter values are of the same order of magnitude of  $\sigma_0$  (see Figure 7b and table III) of the curves in I region (at  $T > 45^\circ\text{C}$ ). The highest value of conductivity of Figure S4 is found for the sample measured at the highest relative humidity. This evidence indicates that some water diffusion could take place through the paraffin covered surface of the pellet. The residual conductivity, measured in these conditions, demonstrates that the charge transport in  $\text{La}_2\text{LiNbO}_6$  pellet is mediated by the amount of water physisorbed on the surface of particle materials.

In II region, in addition to the above discussed chemically bonded water solvation shell, clusters of water are formed on the surface of perovskite, which size and shape are difficult to control in a reproducible way.

The model largely used to interpret conductivity in perovskite type proton conductors, requires the presence of oxide ion vacancies.<sup>41</sup> In order to form proton defects, water gas molecules dissociate into a hydroxide ion that fills an oxygen vacancy and a proton that forms a covalent bond with lattice oxygen. The diffusion of these proton defects needs the diffusion of oxide ion vacancies and thus a high temperature. There is no evidence of oxygen vacancies in  $\text{La}_2\text{LiNbO}_6$  and the small amount of lanthanum observed in B positions can be easily compensated by a small loss of lithium (which is likely to occur) without the need for anion vacancies. The conductivity we observe does not fit into this scheme and the temperature dependence of the low temperature conductivity of  $\text{La}_2\text{LiNbO}_6$  shows a strong increase when temperature diminish in the range 70-25 °C which is not usual for a bulk ionic conductor. Taking all together, the low temperature conductivity registered in proposed material is consistent with typical values of a surface proton transport mechanism. Indeed, the activation energy for the conduction process is 0.22 eV at 25 RH% (Figure S3). This activation energy is compatible with values typical of hydrogen bonding interactions. On this basis, it is easy to conclude that the proton transfer processes occur owing a Grotthus mechanism which takes place by proton exchange events between neighbouring water molecules in physisorbed water domains.

### **3.4.2 Stability, durability, response time and dynamic linearity**

The hysteresis between adsorption and desorption process was also measured in the range of 35–80 RH % (Figure 7-c). The results indicate that the hysteresis falls within  $\pm 5.0$  RH %. The desorption process was located at the top of a loop, indicating that the rate of desorption is slower than that of the adsorption. In order to check the time stability, the sensor was kept during 1 day in the humidity chamber and successively measurements were performed at different times, as is shown in Figure S5-a. Almost no variation in conductivity was observed over 1 day. However the shape of the conductivity vs frequency plot changes, appearing a dispersion in the low frequency area, that could be associated to an electrode polarization phenomenon. This event is probably due to the accumulation of solvated protons at the interface of sample-blocking electrode.



It is worth commenting that all the impedance spectroscopy experiments here reported were performed using the same material in pellet shape, (see Figure S6). It must be outlined that the sample preserved its consistence and shape after all the measurements, thus proving that it is endowed with a very good mechanical stability.

Furthermore, the durability of the material has been studied in more detail by using a sensor based on  $\text{La}_2\text{LiNbO}_6$ , which was operating for one year, and by testing its electric response for one week at  $T= 50\text{ }^\circ\text{C}$  and 50 RH%. Results, shown in Figure S5b, demonstrate that the device based on  $\text{La}_2\text{LiNbO}_6$  after one day of tests is characterized by the same electric response of freshly prepared sensor, thus witnessing its exceptional durability and reproducibility.

The response time of the sensor was determined by measuring on time the conductivity of the material at 1kHz and at different RH% values. Results (see Fig.8a) show that the average response time of the proposed sensor is of 9.52 s. This value is consistent with measurements reported elsewhere for a humidity sensor based on perovskites.<sup>38</sup>

Finally, the ability of the device to follow precisely and in a reproducible way the rapid changes of the RH% parameter was determined by analysing the plot of the dynamic linearity (see experimental section and Fig.8b). Results show that, in the 11-95 RH% range, the dynamic linearity of the sensor is very good, as also witnessed by its correlation factor of  $\chi^2=0.996$  (see Fig. 8b).

#### 4. Conclusions

The high-resolution NPD study of  $\text{La}_2\text{LiNbO}_6$  has shown the material belongs to the group of rock salt ordered double perovskites. The alternation of  $\text{LiO}_6$  and  $\text{NbO}_6$  octahedra occurs in the long range and no cross substitution has been observed. Octahedra are clearly distorted, being  $\text{LiO}_6$  more distorted than  $\text{NbO}_6$ . The octahedra are tilted along the three pseudocubic axes, tilting scheme  $a^-a^+b^+$  in Glazer notation, giving rise to monoclinic symmetry, space group  $P2_1/n$ . The detailed nanostructural analysis performed by scanning transmission electron microscopy has allowed to observe a residual amount of lanthanum in the projected positions of the lithium B-sublattice. The possibility of small cross-substitution La-Li in the A-sublattice was discarded from the electrical

characterization of the material; the conducting properties led us to state that lithium is not a mobile species in this material. The material presented a sensitive response to conductivity with humidity changes and the remarkable low temperature conductivity observed is associated with a surface proton conduction.

The double perovskite prepared from ceramic route seems to present a good performance as humidity-sensor. The conductivity is strongly dependent on the relative humidity, which changes in about 3 orders of magnitude from 25 to 90 RH%. Furthermore, the conductivity remains constant in a wide range of frequency, thus opening the doors to the use of proposed material for devices operating at different frequencies. The analysis of sensitivity parameters as a function of temperature demonstrates that this perovskite is a promising material as sensor at temperatures  $\geq 45$  °C and RH%  $>62\%$ . In addition, the proposed material exhibited in sensing tests a good mechanical stability, durability and hysteresis, with a response time less than 10 s and a very good dynamic linearity range. Finally, the obtained results demonstrate that the conductivity of  $\text{La}_2\text{LiNbO}_6$  occurs between water domains physisorbed on the surface of the sample particles and not owing to charge transfer processes occurring in bulk particles of the material.

### **Conflicts of interest.**

There are no conflicts to declare.

### **Acknowledgments**

We are especially grateful to Professor A.R. West, without whose contributions, suggestions and fruitful discussions this work could not have been carried out. AV would especially like to thank Tony the knowledge received in Solid State Chemistry throughout all the stays in his laboratory along many years. Authors also want to recognise the rich discussions and valuable help of Prof. J. Sanz at ICMN-CSIC, in the structural refinement from neutron diffraction data. This work has been supported by Projects funded by the regional government (Comunidad de Madrid through MATERYENER3CM S2013/MIT-2753) and the Spanish Government, (MICINN through MAT2016-78362-C4-3R and MAT2016-78362-C4-4R). Authors thank the ICTS-Centro Nacional de Microscopia Electrónica (UCM, Madrid) and the ILL (Grenoble) for instrumental facilities. V.D.N.

thanks the University Carlos III of Madrid for the “Cátedras de Excelencia UC3M-Santander” (Chair of Excellence UC3M-Santander).

## References

1. Z. Chen, C. Lu, *Sens. Lett.* 2005, **3**, 274–295.
2. T. A. Blank, L.P. Eksperiandova, K.N. Belikov, *Sensors Actuators B Chem.* 2016, **228**, 416–442.
3. M.R. Mahboob, Z.H. Zargar, T. Islam, *Sensors Actuators B Chem.* 2016, **228**, 658–664.
4. G. Garcia-Belmonte, V. Kytin, T. Dittrich, J. Bisquert, *J. Appl. Phys.* 2003, **94**, 5261-5264.
5. W. Xie, B. Liu, S. Xiao, H. Li, Y. Wang, D. Cai, D. Wang, L. Wang, Y. Liu, Q. Li, T. Wang, *Sensors Actuators B Chem.* 2015, **215**, 125–132.
6. S. A. Krutovertsev, A. E. Tarasova, L. S. Krutovertseva, and A. V. Zorin, *Sens. Actuators A* 62, 582 (1997).
7. G. Gusmano, G. Montesperelli, and E. Traversa, *Sens. Actuators B* 7, 460 (1992).
8. K. Arshaka, K. Twomey, and D. Egan, *Sensors* 2, 50 (2002).
9. Y. Zhang, X. Zheng, T. Zhang, L. Gong, S. Dai, Y. Chen, *Sensors Actuators B Chem.* 2010, **147**, 180–184.
10. Z. Imran, S.S. Batool, H. Jamil, M. Usman, M. Israr-Qadir, S.H. Shah, et al., *Ceram. Int.* 2013, **39**, 457–462.
11. Y. He, X.W. Liu, R. Wang, T. Zhang, *Sens. Lett.* 9 (2011) 262–265
12. M.A. Hassen, A.G. Clarke, M.A. Swetnam, R.V. Kumar, D.J. Fray, *Sens. Actuators B*, 69 (2000), 138-143.
13. Minghua Zhou, Aftab Ahmad, *Sens. Actuators B*, 129 (2008), 285-291.
14. XiaoXin Chen, Loren Rieth, Mark S. Miller, Florian Solzbacher, *Sens. Actuators B*, 148 (2010), pp. 173-180.
15. J. P. Lucaszewicz, *Sens. Actuators B* 4, 227 (1991).
16. M. Viviani, M. T. Buscaglia, V. Buscaglia, M. Leoni, and P. Nanni, *J. Euro. Ceram. Soc.* 21, 1981 (2001).
17. Y.D. Zhang, X.M. Pan, Z. Wang, Y.M. Hu, X.Y. Zhou, Z.L. Hu, H.S. Gu, *RSC Adv.* 5 (2015) 20453–20458.

18. Y. Zhen, M. Wang, S. Wang, Q. Xue, *Ceram. Int.* 40 (2014) 10263–10267.
19. M. Yuan, Y. Zhang, X. Zheng, B. Jiang, P. Li, S. Deng, *Sens. Actuators B* 209 (2015) 252–257.
20. G-J Ji, L-X Zhang, M-Y Zhu, S-M Li, J. Yin, L-X Zhao, B. D. Fahlman, L-J Bie, *Ceramics International* 44 (2018) 477–483.
21. T. Seiyama, N. Yamazoe, H. Arai, *Sens. Actuators.* 4 (1983), 85–96.
22. T. Nitta, in *Chemical Sensor Technology Vol 1*, Editor T. Seiyama, Kodansha Ltd. Tokyo, Elsevier, 1988, **1**, 57-78.
23. J. Tortelier, P. Gougeon, *Acta Crystallogr. Sect. C Cryst. Struct. Commun.* 1996, **52**, 500–502.
24. S., Vasala, M. Karppinen, *Progress in Solid State Chemistry* 2015, **43**, 1-36
25. S. Narayanan, F. Ramezanipour, V. Thangadurai, *J. Phys. Chem. C*, 2012, **116**, 20154–20162.
26. Roger H. Mitchell, *Perovskites. Modern and Ancient*, Almaz Press (Ontario, Canada) 2002
27. H. M. Rietveld, *J. Appl. Crystallogr.* 1969, **2**, 65– 71.
28. J. Rodríguez-Carvajal, *Physica B*, 1993, **192**, 55–69
29. Zview 2 for Windows (Version 2.0). Scribner Assoc. Inc., Charlottesville, VA, USA (2000)
30. P. A. Seinen, F. P. F. Vanberkel, W. A. Groen, D. J.W. Ijdo, *Mater. Res. Bull.* 1987, **22**, 535–542.
31. R.D. Shannon, C.T. Prewitt, *Acta Crystallogr. B*, 1969, **25**, 222.
32. M. T., Anderson, K. B., Greenwood, G. A. Taylor, K. R Poepfelmeier, *Prog. Solid State Chem.* 1993, **22**, 197-233.
33. A. R. West, *Solid state chemistry and its applications*, John Wiley & Sons, USA, 2007.
34. A.D. Robertson , A.R. West , A.G. Ritchie, *Solid Stat. Ionics*, 1997, **104**, 1–11
35. A. Boulant, P. Maury, J. Emery, J-Y. Buzare, and O. Bohnke, *Chem. Mater.*, 2009, **21**, 2209–2217.
36. T. Durán, E. Climent-Pascual, M.T. Pérez-Prior, B. Levenfeld, A. Varez, I. Sobrados and J. Sanz, *Adv. Powder Technol.* 2017, **28**(2), 514-520.
37. L. Truong and V. Thangadurai, *Inorg. Chem.* 2012, **51**, 1222–1224.
38. G-J Ji, L-X Zhang, M-Y Zhu, S-M Li, J. Yin, L-X Zhao, B.D. Fahlman and L-J Bie, *Ceram. Int.* 2018, **44**, 477-483

39. G. Chiodelli, F. Maglia, U. Anselmi-Tamburini, Z.A. Munir, *Solid State Ionics* 2009, **180**, 297-301.
40. C. Tandé, D. Pérez-Coll, G. Mather, *J. Mater. Chem.*, 2012, **22**, 11208-11213.
41. K.D. Kreuer, *Annu. Rev. Mater. Res.* 2003, **33**, 333–59.

**Table I.** Atomic Coordinates, Occupancy Factors, and Equivalent Isotropic Displacement Parameters for  $\text{La}_2\text{LiNbO}_6$  refined in  $P2_1/n$  space group.

<b>3.5 K</b>						
Atom	Wyckoff	x	y	z	$B_{\text{iso}} (\text{Å}^2)$	Occupancy
Li(1)	2c	0	½	0	0.33(3)	0.99
Li(2)	2d	½	0	0	0.092(9)	0.01
Nb(1)	2d	½	0	0	0.092(9)	0.98
Nb(2)	2c	0	½	0	0.33(3)	0.02
La	4e	0.50837(7)	0.55249(5)	0.25395(4)	0.188(5)	
O1	4e	0.2129(1)	0.18765(9)	-0.04574(6)	0.320(9)	
O2	4e	0.30987(9)	0.71631(9)	-0.04971(6)	0.51(1)	
O3	4e	0.40709(9)	0.97296(8)	0.24103(6)	0.253(8)	
<b>293 K</b>						
Atom	Wyckoff	x	y	z	$B_{\text{iso}} (\text{Å}^2)$	Occupancy
Li	2c	0	½	0	0.96(2)	
Nb	2d	½	0	0	0.577(4)	
La	4a	0.50852(7)	0.55122(5)	0.25362(5)	0.615(2)	
O1	4e	0.2139(1)	0.1877(1)	-0.04593(7)	0.954(5)	
O2	4e	0.31162(9)	0.71247(9)	-0.04952(6)	0.828(6)	
O3	4e	0.40633(8)	0.97291(8)	0.23896(6)	0.685(4)	

**Table II.** Cell Constants and Refinement Parameters of La<sub>2</sub>LiNbO<sub>6</sub>.

	3.5 K	293K
<b>a (Å)</b>	5.6027(1)	5.61612(2)
<b>b (Å)</b>	5.7627(1)	5.76653(2)
<b>c (Å)</b>	7.9196(2)	7.94102(3)
<b>β (°)</b>	89.688(2))	89.724(2)
<b>V (Å<sup>3</sup>)</b>	255.691(9)	257.171(2)
<b>Z</b>	2	2
<b>R<sub>B</sub></b>	6.15	6.98
<b>R<sub>F</sub></b>	3.73	4.39
<b>R<sub>wp</sub></b>	5.59	5.86
<b>R<sub>p</sub></b>	4.32	4.42
<b>χ<sup>2</sup></b>	0.592	0.611
<b>d<sub>Li-O1</sub> (Å)x2</b>	2.1884 (5)	2.1945(5)
<b>d<sub>Li-O2</sub> (Å)x2</b>	2.1715 (5)	2.1707(5)
<b>d<sub>Li-O3</sub> (Å)x2</b>	2.1244 (5)	2.1468(6)
<b>d<sub>Nb-O1</sub> (Å)x2</b>	1.9735 (5)	1.9725(5)
<b>d<sub>Nb-O2</sub> (Å)x2</b>	1.9917 (5)	2.0068(5)
<b>d<sub>Nb-O3</sub> (Å)x2</b>	1.9820 (5)	1.9729(6)
<b>d<sub>La-O1</sub> (Å)</b>	3.5830(6)	3.5815
	2.7297(6)	2.7461
	2.7153(6)	2.7186
	2.4008(6)	2.4044
<b>d<sub>La-O2</sub> (Å)</b>	2.8180(6)	2.8121
	3.5174(6)	3.5396
	2.4567(6)	2.4379
	2.6598(6)	2.6878
<b>d<sub>La-O3</sub> (Å)</b>	3.3891(6)	3.3860
	2.4908(6)	2.5013
	2.3725(6)	2.3737
	3.3074(6)	3.3180

**Table III.**  $\sigma_0$ (S·cm<sup>-1</sup>) and  $S = \frac{\partial \log(\sigma)}{\partial R.H. \%}$  fitting parameters determined by simulating the conductivity data of Figure 7a with Equation 3. The goodness of the fit is expressed in term of  $\chi^2$  coefficient.

<b>T</b> <b>/°C</b>	<b>I</b>			<b>II</b>		
	<b>σ<sub>0</sub>(S·cm<sup>-1</sup>)</b>	<b><math>\frac{\partial \log(\sigma)}{\partial R.H. \%}</math></b>	<b>χ<sup>2</sup></b>	<b>σ<sub>0</sub>(S·cm<sup>-1</sup>)</b>	<b><math>\frac{\partial \log(\sigma)}{\partial R.H. \%}</math></b>	<b>χ<sup>2</sup></b>
30	7.6·10 <sup>-10</sup> ±3.3·10 <sup>-11</sup>	0.051±5.5·10 <sup>-04</sup>	1.000	1.0·10 <sup>-08</sup> ±7.2·10 <sup>-10</sup>	0.034±1.5·10 <sup>-03</sup>	0.994
40	3.0·10 <sup>-10</sup> ±4.4·10 <sup>-11</sup>	0.056±1.8·10 <sup>-03</sup>	0.998	5.1·10 <sup>-09</sup> ±2.5·10 <sup>-10</sup>	0.036±1.1·10 <sup>-03</sup>	0.997
50	1.3·10 <sup>-09</sup> ±1.3·10 <sup>-10</sup>	0.049±1.3·10 <sup>-03</sup>	0.999	2.0·10 <sup>-08</sup> ±3.9·10 <sup>-10</sup>	0.031±4.2·10 <sup>-04</sup>	0.999
60	1.5·10 <sup>-09</sup> ±7.8·10 <sup>-11</sup>	0.049±6.4·10 <sup>-04</sup>	1.000	2.8·10 <sup>-08</sup> ±7.7·10 <sup>-10</sup>	0.029±5.9·10 <sup>-04</sup>	0.999
70	1.5·10 <sup>-09</sup> ±9.3·10 <sup>-11</sup>	0.049±7.8·10 <sup>-04</sup>	1.000	2.8·10 <sup>-08</sup> ±5.7·10 <sup>-10</sup>	0.030±4.3·10 <sup>-04</sup>	0.999